Acta Geologica Sinica (English Edition), 2024, 98(6): 1557–1573

Fracture Effectiveness and its Influence on Gas Productivity in Ultra-deep Tight Sandstone Reservoirs of the Keshen Gas Field, Tarim Basin

XU Xiaotong[1, 2], ZENG Lianbo[1, 2, *], DONG Shaoqun[3], DIWU Pengxiang[3], LI Haiming[4], LIU Jianzhong[4], HAN Gaosong[5], XU Hui[6] and JI Chunqiu[4]

[1] *State Key Laboratory of Petroleum Resources and Engineering, China University of Petroleum (Beijing), Beijing 102249, China*
[2] *College of Geoscience, China University of Petroleum (Beijing), Beijing 102249, China*
[3] *College of Science, China University of Petroleum (Beijing), Beijing 102249, China*
[4] *Tarim Oilfield Company, PetroChina, Korla, Xinjiang 841000, China*
[5] *SINOPEC Northwest Oil Field Company, Urumqi 830011, China*
[6] *Shenzhen Branch of CNOOC Ltd., Shenzhen 518000, China*

Abstract: Fracture effectiveness plays a key role in gas productivity of ultra-deep tight sandstone reservoirs, Kuqa depression, Tarim Basin. Based on cores, thin sections, well logging, well testing and production data, the study evaluated fracture effectiveness and illustrated its impacts on gas productivity. High-angle and vertical shear fractures are the most important types. Distribution of effective fractures shows great heterogeneous. Fracture effectiveness is influenced by tectonism, diagenesis and in-situ stress. Earlier fractures or fractures in close to gypsum rock are easier to be filled. Completely filled fractures can be reopened under late tectonism. Dissolution improves local fracture effectiveness. Minerals spanning fracture surfaces protect fracture effectiveness from late compression. Fractures filled with calcite can be activated by acidification. Effective fractures parallel to maximum horizontal principal compressive stress direction show larger aperture. Overpressure can decrease the effective normal stress to maintain fracture effectiveness. With exploitation, decline in pore pressure reduces fracture effectiveness. Linear density, aperture, and strike of effective fractures influence gas productivity. Effective fractures greatly enhance matrix permeability. Therefore, more abundant and larger aperture fractures are always corresponded to higher productivity. However, effective fractures also facilitate late water invasion, especially, both mutually parallel. Intense water invasion leads to rapidly declines in productivity.

Key words: tectonic fracture, fracture effectiveness, gas productivity, ultra-deep tight sandstone, Kuqa depression

Citation: Xu et al., 2024. Fracture Effectiveness and its Influence on Gas Productivity in Ultra-deep Tight Sandstone Reservoirs of the Keshen Gas Field, Tarim Basin. Acta Geologica Sinica (English Edition), 98(6): 1557–1573. DOI: 10.1111/1755-6724.15259

1 Introduction

Ultra-deep reservoirs exhibit abundant resources, and are crucial domains for hydrocarbon exploration and exploitation (Cao B F et al., 2022). Based on Chinese exploration practice, the "ultra-deep" exhibits burial depth exceeding 4500 m in the east, while the burial depth exceeding 6000m is defined the "ultra-deep" in the west (Jia, 2023). Tight sandstone gas reservoir is characterized by a gas-bearing sandstone formation with overburden porosity of less than 10%, permeability below 0.1×10^{-3} μm^2, and gas saturation not exceeding 60% (Jia et al., 2012). Due to multiple interaction between tectonism, fluid and rock, ultra-deep reservoirs exhibit low matrix physical property, complex diagenesis, natural fracture enrichment, as well as pronounced heterogeneity (Bloch et al., 2002; Bjørlykke, 2014; Cao B F et al., 2017, 2020, 2024; Zhang L K et al., 2021; Xu et al., 2023; Zeng et al., 2023a). Natural fractures can significantly enhance reservoir performance and seepage ability of ultra-deep reservoirs (Cao B F et al., 2021; Rashid et al., 2023; Zeng et al., 2023a; Cao D S et al., 2024). With fluid potential decreasing, oil and gas can rapidly migrate and accumulate along fractures (Zeng et al., 2010; Shen et al., 2017). Accordingly, domains abundant in natural fractures are endowed with copious reserves of oil and gas (Zeng et al., 2022; Du et al., 2023). However, with exploitation, declines in pore pressure is preferentially transmitted along fractures (Zhou et al., 2021; Lü et al., 2022). Fractures serve as high-speed pathways for water invasion, resulting in a rapidly decline in productivity (Jia et al., 2019; Liu Q M et al., 2023).

Influenced by tectonism, diagenesis, fluid and so on, fracture effectiveness undergoes a complex dynamic evolution (Laubach and Ward, 2006; Laubach et al., 2016). Fracture effectiveness refers to the degree to which fractures remain open and provide space for fluid flow

* Corresponding author. E-mail: lbzeng@sina.com

under overburden conditions (Laubach, 2003). Effective fractures facilitate rapid fluid migration, while ineffective ones impede it (Nelson, 2001; Liu et al., 2021). Therefore, the evaluation of fracture effectiveness is significant for efficient exploration and exploitation of ultra-deep reservoirs. At present, in terms of lithology, mechanical stratigraphy, tectonism, diagenesis, and in-situ stress, development and effectiveness of fractures are comprehensively evaluated (Laubach et al., 2004a, 2009; Lyu et al., 2022; Lai et al., 2023a; Liu G P et al., 2023). For example, combined with microthermometry of fluid inclusion and creak-seal texture, the time-dependent evolution of fracture effectiveness is quantitatively evaluated (Becker et al., 2010; Lander and Laubach, 2015; Laubach et al., 2019). Distribution patterns of fractures in various structural units are analyzed through finite element numerical simulation and discrete element numerical simulation (Sun et al., 2018; Feng et al., 2019; Wang Z et al., 2020; Zhang R H et al., 2021; Zeng et al., 2024). However, influence by multiple tectonism–diagenesis interaction, fracture effectiveness shows extremely heterogeneous (Laubach et al., 2010; Zeng et al., 2016; Wang et al., 2023). Heterogeneous fractures exert profound influences on productivity. Especially for ultra-deep reservoirs, productivity fluctuations signify inherent controls by fracture effectiveness. Therefore, comprehensive evaluation of fracture effectiveness is important for the policy-making of water prevention and control, and gas productivity improvement.

The Keshen gas field is a crucial exploration and exploitation zone in the Kuqa depression (Zhang R H et al., 2021; Wang et al., 2023a). It exhibits ultra-burial depth, ultra-high pressure and temperature, dense matrix, natural fractures enrichment, intricate gas-water distribution, and edge and bottom water development (Zhang R H et al., 2014; Zhao et al., 2018; Jia et al., 2019). Natural fractures greatly enhance reservoir performance and seepage capacity, and play a key influence on gas productivity (Wang et al., 2018, 2023b; Zhang R H et al., 2021; Xia et al., 2024). However, influenced by severe water invasion, certain gas reservoirs have been flooded, leading to a rapid decline in gas productivity (Wei et al., 2019). As fast channels for water invasion, natural fractures play a vital role. Current researches are mainly focused on fracture types, development characteristics, controlling factors, and distribution patterns (Gong et al., 2015, 2017; Li et al., 2017; Wang et al., 2021). The influencing factors, distribution laws, and productivity control of effective fractures have been the subject of limited researches. Based on cores, thin sections, well logging, the characteristics and distribution of effective fractures were analyzed. Combined with production data, factors on fracture effectiveness were evaluated. Ultimately, the effects of fracture effectiveness on gas productivity were illustrated. The study provides guidance for efficiently exploitation and water prevention and control of ultra-deep tight gas reservoirs.

2 Geological Setting

2.1 Location and structure

The Kuqa depression is situated on the northern Tarim Basin, northwest China (Fig. 1a). It is a Meso-Cenozoic superimposed foreland basin that developed on the passive continental margin of the Paleozoic era. Since late Hercynian period, it has undergone foreland basin, depression basin, flexural basin, and intracontinental foreland basin (He, 2022). The Kuqa depression extends in the NEE direction, with an area of approximately $2.85 \times 10^4\,km^2$. It consists of the northern monoclinal belt, the Kelasu structural belt, the Yiqikelike structural belt, the Qiulitage structural belt, along with the southern slope belt and the Yangxia depression and Baicheng depression (Fig. 1a). Influenced by intense tectonic compression, the Kelasu structural belt is oriented in the NEE–SWW direction. The fault system predominantly consists of imbricated thrust faults. The Kelasu structural belt exhibits abundant resources, with successive discoveries made in the Kela 2, Dabei, Keshen and Bozi gas fields.

The Keshen gas field, as a thrust nappe structure, was formed during the Meso-Cenozoic era. Influenced by the nearly N–S striking compression and nappe movement, the extrusion deformations occurred in the northern Keshen gas field, and then spread towards the south (Wei et al., 2020). The diverse tectonic compressions have given rise to various fault-anticline systems (Fig. 1b, c) (Qi et al., 2023). The exceptional geological conditions of gas accumulation exhibit a promising exploitation prospect.

2.2 Stratigraphy

Drilling reveals that the strata comprise the Lower Cretaceous Baxigai Formation (K_1bx) and Bashijiqike Formation (K_1bs), the Paleogene Kumugeliemu Group ($E_{1-2}km$) and Suweiyi Group ($E_{2-3}s$), the Neogene Jidike Formation (N_1j), Kangcun Formation ($N_{1-2}k$) and Kuche Formation (N_2k), and the Quaternary (Q) (Fig. 2). The K_1bs is the most dominant gas-bearing formation. It is in conformity contact with the K_1bx and unconformity contact with the $E_{1-2}km$. The Triassic and Jurassic lacustrine coal strata are source rocks. They exhibit substantial thickness, exceptional maturity, and remarkable hydrocarbon generation intensity. The thick gypsum rock in the $E_{1-2}km$ serves as superior regional cap rock.

The K_1bs is vertically classified into K_1bs^1, K_1bs^2, and K_1bs^3. Influenced by the late Cretaceous tectonic uplift, the entire upper Cretaceous and partial K_1bs^1 underwent denudation. During the sedimentary period of the K_1bs, sediments originated from the southern Tianshan orogenic belt. Sediments swiftly cascaded into the lake and gave rise to a giant fan-shaped deposit. The K_1bs^1 and K_1bs^2 exhibit the braided river delta front, while the K_1bs^3 showcases the fan delta front. The giant thick sand body extends far and is evenly distributed across a vast expanse (Zhang H L et al., 2014).

2.3 Reservoir

The K_1bs is buried at a depth ranging from 6150 m to 6750 m, with average thickness from 300 m to 330 m. The lithology is predominantly reddish-brown medium and fine-grained lithic feldspar sandstone, followed by the feldspar lithic sandstone. Controlled by early long-term shallow burial and later rapidly deep burial, a portion of the primary intergranular pores are preserved in the

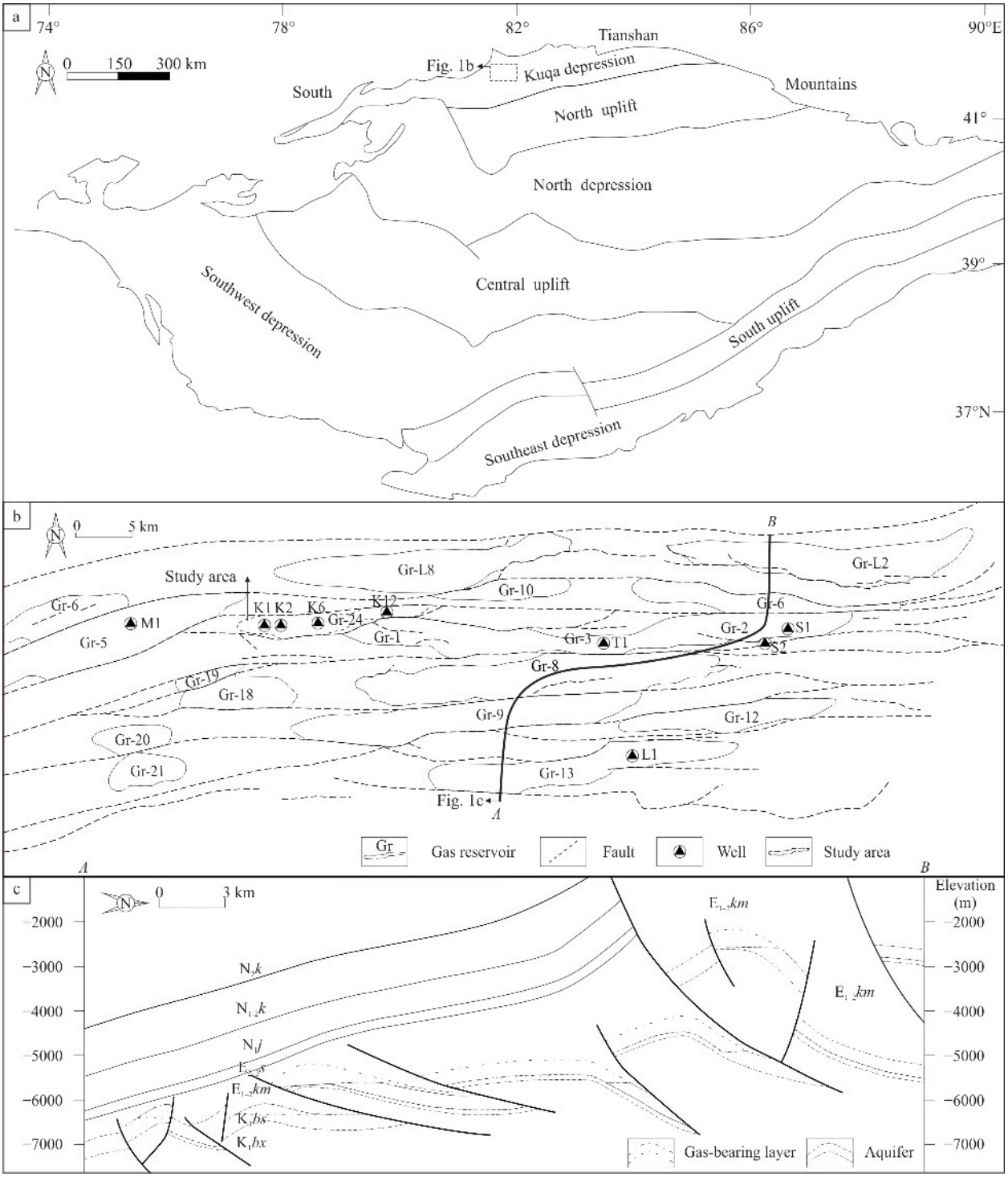

Fig. 1. (a) Location and structural units of the Tarim Basin (modified from Guo et al., 2016 and Zeng et al., 2023b); (b) structural plane of the Keshen gas field (modified from Wang et al., 2023a); (c) structural profile of the Keshen gas field (modified from Zhang R H et al., 2021).

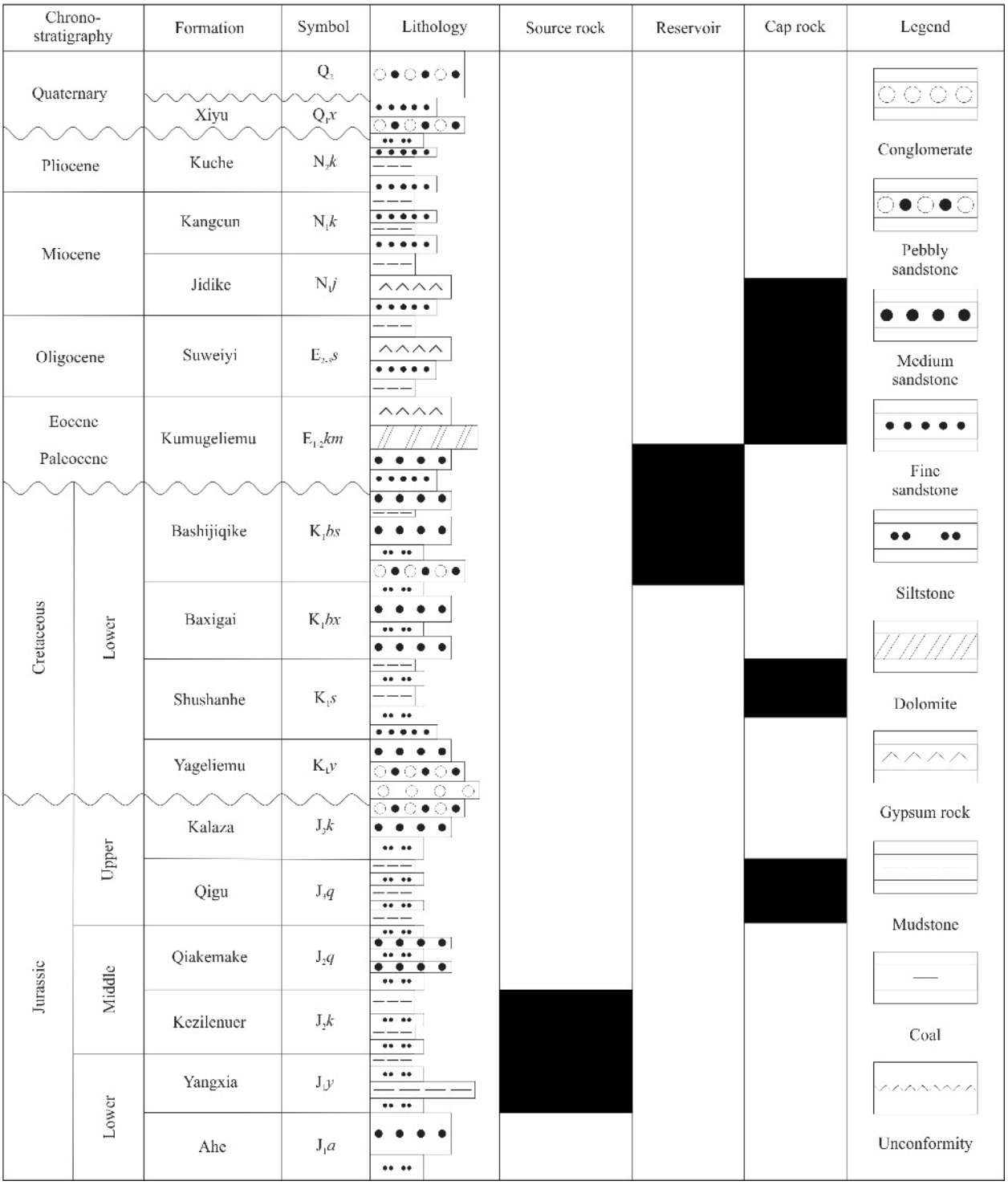

Fig. 2. The comprehensive stratigraphic column of the Keshen gas field.

reservoir (Liu et al., 2021). Pore types are mainly primary intergranular pores and intergranular pores, micro-pores and micro-fractures. Measured matrix porosity and permeability range from 0.5% to 9.66% and from 0.01 × 10^{-3} μm^2 to 0.1 × 10^{-3} μm^2, respectively. As a whole, it is a typical ultra-deep tight sandstone reservoir.

3 Samples and Methods

In this study, cores were from wells K1, K2, K6, and K12, with a total length 55.88 m. Cores were meticulously observed and comprehensively described. The statistical data included fracture types, dip angle (horizontal fracture: 0–15°, low-angle fracture: 15°–45°, high-angle fracture:

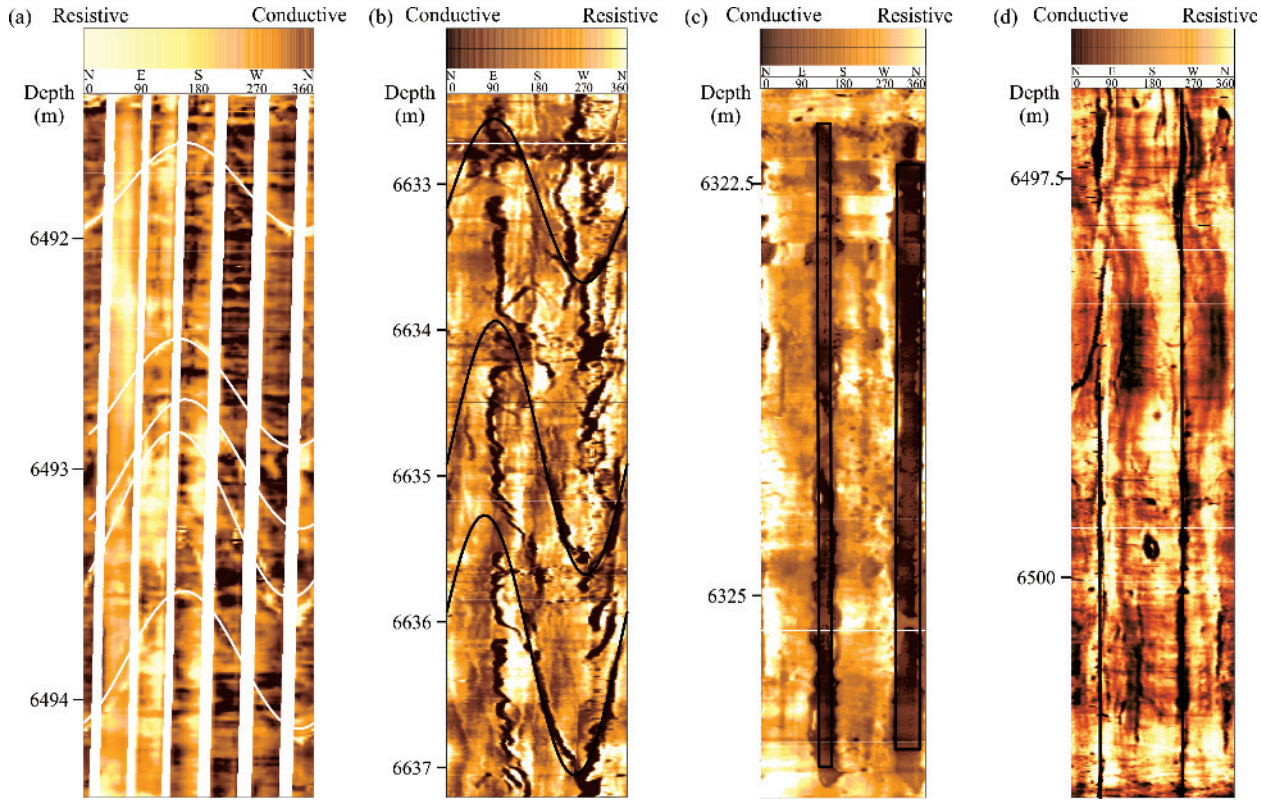

Fig. 3. The interpretation results of borehole image logs.
(a) Ineffective fractures of electrical image log; (b) effective fractures of ultrasonic image log; (c) borehole breakouts of ultrasonic image log; (d) induced fractures of ultrasonic image log.

45°–75°, vertical fracture: 75°–90°) (Wang K et al., 2020), aperture, filling degree (unfilled fracture, partially filled fracture, completely filled fracture) (Laubach et al., 2004b; Gale et al., 2010), filling minerals types and crosscutting relationship. Subsequently, 20 samples were selected for making thin sections in order to observe microscopic characteristics. Each thin section was stained with a mixture of alizarin red and potassium ferricyanide, in order to differentiate between various carbonate minerals. Linear density and aperture were employed to characterize fracture development degree. Linear density denotes the quantity of fractures per unit length. Aperture was determined by employing the calculation method and model based on dual laterolog data proposed by Li et al (2008). The aperture of microscopic fractures was measured using the AxioVision Rel.4.8 software.

Borehole image logs consist of electrical image logs for 8 wells and ultrasonic image logs for 11 wells. All gas wells are vertical wells and are injected with oil-based drilling mud. This study defines unfilled and partially filled fractures as effective fractures, while completely filled ones refer to ineffective fractures (Laubach, 2003). For electronic image logs in oil-based drilling mud, effective fractures exhibit black low-resistance sinusoids, ineffective ones appear as bright high-resistance sinusoids (Fig. 3a). Ineffective fractures are often filled by high-resistance minerals like calcite (Aghli et al., 2020; Liu et al., 2021). For ultrasonic image logs, effective fractures exhibit complete dark sinusoids (Fig. 3b), whereas ineffective fractures present incomplete dark sinusoids (Lai et al., 2017). Efficacy of ultrasonic image logs in fracture detection in oil-based drilling mud is more remarkable. This study preferentially adopts results of ultrasonic image logs, complemented by those of electrical image logs. The maximum/minimum horizontal principal compressive stress direction ($D\sigma_H/D\sigma_h$) is determined by the orientation of borehole breakouts or induced fractures identified (Fig. 3c, d). The orientation of borehole breakouts is parallel to the $D\sigma_h$. The orientation of induced fractures is parrel to the $D\sigma_H$ (Zeng et al., 2019; Chatterjee and Mukherjee, 2023).

4 Results

4.1 Natural fracture development characteristics

Natural fractures in the Keshen gas field can be categorized into tectonic fracture, diagenetic fracture, and overpressure fracture (Fig. 4) (Liu et al., 2021; Zeng et al., 2023b). Tectonic fracture is the primary type. Tectonic fractures are mainly shear fractures, followed by tensile fractures. Shear fractures always extend vertically for several meters and exhibit trans-layer development. The fracture surface appears flat and straight, with occurrence of scratches and steps (Fig. 4a). Multiple shear fractures frequently crosscut reciprocally (Fig. 4b). Microscope shear fractures exhibit a range of apertures spanning from tens to hundreds of microns. Partial grains flanking fracture surfaces can be dissolved (Fig. 5a). Fracture can

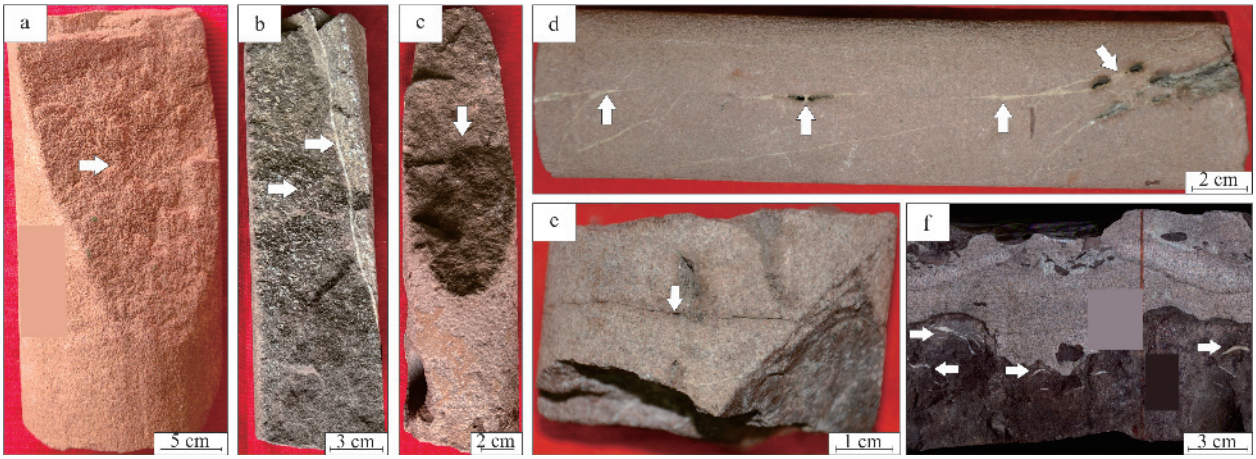

Fig. 4. Macroscopic photos of typical natural fractures in the cores.
(a) High-angle shear fracture and steps, well K6, 6448.1–6448.19 m, K_1bs; (b) partially filled fracture crosscuts completely filled one, well K6, 6565.3–6565.55 m, K_1bs; (c) unfilled tensile fracture, well K6, 6564.05–6565.28 m, K_1bs; (d) partially filled and completely filled tensile fractures and localized mineral bridges, well S1, 6512.59–6512.83 m, K_1bs; (e) bedding fracture, well S2, 6990–6990.04 m, K_1bs; (f) overpressure fractures, well K6, 6441.4–6441.56 m, K_1bs.

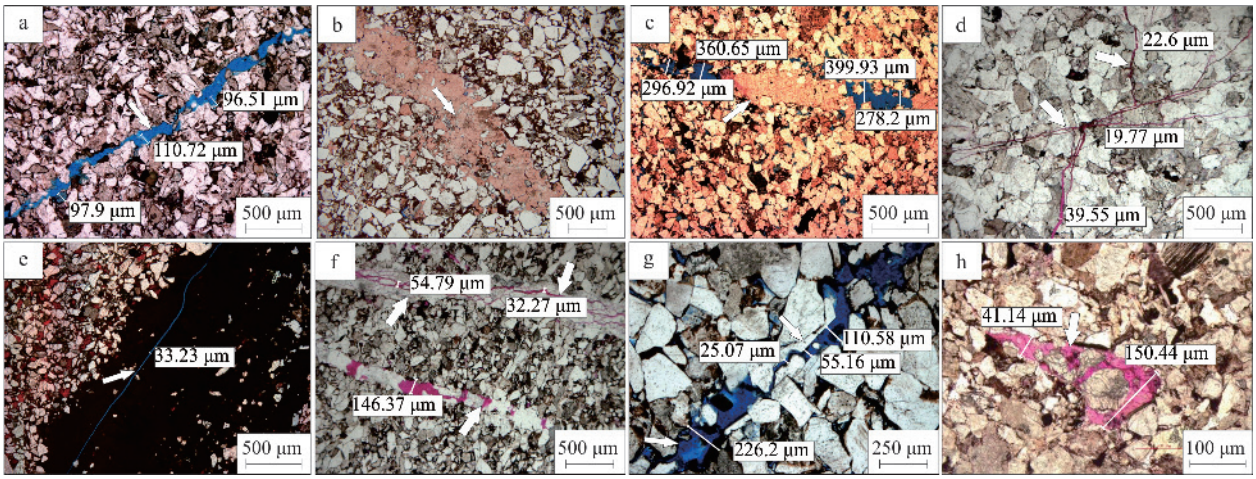

Fig. 5. Microscopic photos of typical natural fractures.
(a) Shear fracture, with dissolved grains flanking the surfaces, well K6, 6568.95 m, K_1bs; (b) shear fracture is completely filled with calcite, well K2, 6444.34 m, K_1bs; (c) tectonic fracture is partially filled by dolomite, well K6, 6446.94 m, K_1bs; (d) multi-stage transgranular fractures, well T1, 6951.49 m, K_1bs; (e) bedding fracture, well K2, 6512.07 m, K_1bs; (f) completely filled fracture is reopened, giving rise to new fractures, and the fracture is partially filled by siliceous, well T1, 6884.95 m, K_1bs; (g) quartz overgrowth flanking the shear fracture surface, well L1, 7345.71 m, K_1bs; (h) Completely filled fracture is dissolved locally, well S1, 6512.02 m, K_1bs.

be filled by various minerals such as calcite, silica, anhydrite (Fig. 5b, f). Tensile fracture often vertically extends lengths ranging from centimeters to decimeters. It always terminates at the layer interface. Tensile fracture surface is always uneven (Fig. 4c). Although, its aperture is always large, while it is susceptible to being filled by minerals such as calcite (Fig. 4d). Microscope tensile fracture consistently circumvents grains and is partially filled with dolomite (Fig. 5c). Hence, grains flanking tensile fracture surface remain intact. Transgranular fracture is also observable under the microscope (Fig. 5d). Its aperture ranges from nanometers to tens of microns. Influenced by grain fabric, it usually extends through or around grains. Multiple transgranular fractures exhibit crosscutting relationships.

Diagenetic fracture observed is bedding fracture (Fig. 4e). Bedding fracture typically develops parallel to layer interface. Its aperture ranges from nanometers to tens of microns. Microscope bedding fracture develops along micro-bedding surface (Fig. 5e). It usually displays limited transverse continuity, discontinuous distribution. The formation of bedding fracture is related to pressure dissolution and abnormal fluid pressure (Bons et al., 2012; Cobbold et al., 2013). Overpressure fracture occurs when the internal fluid pressure within rock surpasses tensile strength (Zeng et al., 2023a). Overpressure fractures typically have a limited extension, with distinct variations in occurrence (Fig. 4f). These fractures often exhibit lenticular shapes and are prone to being completely filled with minerals.

Based on cores and borehole image logs, dip angle of tectonic fractures ranges between 30° and 90°, mainly

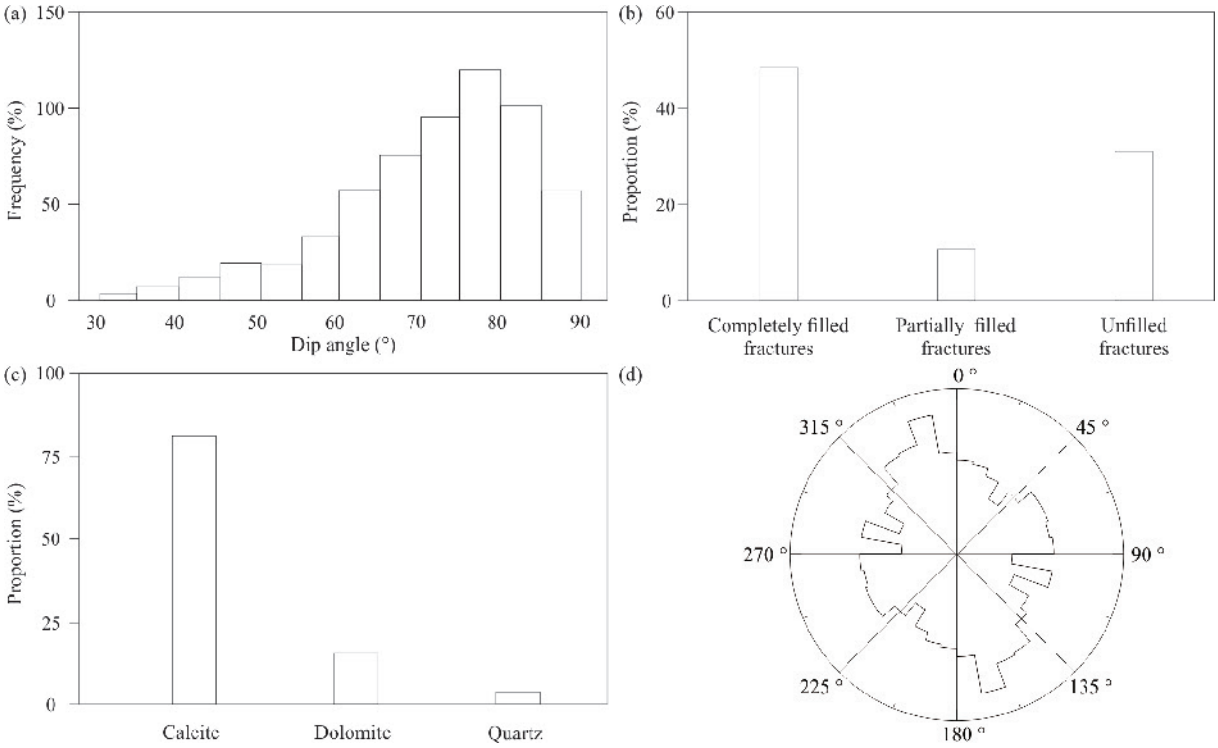

Fig. 6. Development characteristics of tectonic fractures.
(a) Dip angle; (b) filling degree; (c) filling types; (d) rose diagram of strike.

characterized by high angle and vertical fractures (Fig. 6a). The completely filled fractures are primarily, accounting for 48%; unfilled fractures come second at 36%, while partially filled ones make up a smaller proportion at 16% (Fig. 6b). Tectonic fractures are mainly filled by calcite, constituting approximately 78%, followed by dolomite and quartz (Fig. 6c). Tectonic fractures mainly exhibit the N–S, NEE–SWW, NWW–SEE, as well as nearly E–W strikes (Fig. 6d).

4.2 Distribution laws of effective fractures

The distribution of effective fractures exhibits heterogeneity (Fig. 7). Effective fractures exhibit the N–S, NE–SW, NNE–SSE, and nearly E–W strikes. As a whole, the fracture strike is primarily influenced by the paleotectonic stress (Zeng et al., 2004). However, it can be altered by local faults and folds.

Horizontally, the linear density of effective fractures ranges from 0.04 m^{-1} to 0.356 m^{-1}, with an average of 0.177 m^{-1} in the western gas reservoir and 0.194 m^{-1} in the eastern. In the western, the effective fractures appear as the N–S strike. Gradually it is transformed to the NW–SE strike around well K4. In the eastern, the effective fracture strike has gradually transformed from the NEE–SWW strike to the NNE–SSW strike. Subsequently, it shifts towards the NNW–SSE strike in proximity to well K14.

Vertically, the linear density of effective fractures in K_1bs^1 is comparatively lower than that in K_1bs^2. Meanwhile, no effective fractures are abundant in the lower K_1bs^1 in wells K1 and K8, and in the whole K_1bs^1 of well K2. Compared with the upper K_1bs^2, the effective fractures are more abundant in the middle-lower K_1bs^2. Overall, there is a certain stratification for the effective fracture strike. It transitions from the nearly E–W and NEE–SWW strike in the K_1bs^1 to the nearly N–S and NNW–SSE strike within the K_1bs^2.

5 Discussions

5.1 Influencing factors of fracture effectiveness

5.1.1 Tectonism

Tectonism plays a key role on fracture effectiveness. Controlled by multiple tectonic movements, various tectonic fractures exhibit intercutting, dislocation, spatial confinement, and varying degrees of filling. Notably, the completely filled fracture is subsequently crosscut by the partially filled fracture (Fig. 4b). It can be inferred that fracture generated earlier has undergone long-term diagenesis and thus exhibits greater tendence for mineral infilling (Liu et al., 2021). As a whole, the tectonic fractures in the Keshen gas field can be categorized into three stages (Zeng et al., 2004; Wei et al., 2020). They are the nearly E–W striking fractures during the late Yanshan period, the nearly N–S striking fractures during the middle Himalayan period, and a few nearly E–W striking fractures along with the predominant nearly N–S striking fractures in the late Himalayan period. Based on results of borehole image logs, the ineffective fractures mainly exhibit the nearly E–W and NWW–SEE strikes (Fig. 8a), and the effective fractures mainly appear as the NNW–SSE, nearly N–S and NNE–SSW strikes (Fig. 8b). As a result, the nearly E–W striking fractures are more susceptible to be filled.

Fracture effectiveness is also influenced by late tectonic

compression or uplift (Zeng et al., 2010). Influence by late tectonic movements, the previously completely filled fracture is reopened, accompanied with the development of new fractures (Fig. 5f). The aperture of new fractures ranges from 32.27 to 54.79 μm. Meanwhile, the dissolution of grains can be observed on the new fracture surface. It indicates that the reopened fracture serves as pathways for late-stage fluid migration.

5.1.2 Diagenesis

Natural fractures can serve as pathways for fluid migration and spaces for various fluid–rock interactions. Conversely, various fluid–rock interactions significantly influence fracture effectiveness. Fracture effectiveness is diminished as mineral deposits precipitate through cementation (Laubach and Ward, 2006; Cao et al., 2023). Vertically, the K_1bs^1 is in an unconformable contact with the overlying gypsum rock. Hence, multiple diagenetic fluids permeate into the reservoir through the unconformity and pore–fracture network (Hudec and Jackson, 2007; Wei et al., 2020; Yang et al., 2022). As a result, within the distance of 100 m from the unconformity, there is a prevalence of filled fractures, accounting for 35%–40%. As the distance increases, the proportion gradually diminishes to 24%–28%. Beyond the distance of 200 m, the unfilled fractures are predominant, with less than 10% being filled (Fig. 9). Additionally, influenced by completely filled with calcite, dolomite, or anhydrite, microscope effective fractures are transformed into ineffective fractures (Fig. 5b, f). Besides being reopened due to the influence of subsequent tectonic movements, these fractures also function as barriers, hindering the migration of fluids. It can also be observed that quartz and albite flanking the fracture surface undergo overgrowth. The overgrowth results in localized narrowing and frequent variations in aperture that range from 25.07 μm to 226.2 μm (Fig. 5f).

In general, cementation can diminish fracture effectiveness. Notably, the local cementation may effectively prevent fractures from closures caused by later tectonic compression (Laubach, 2003). It can be observed in the core that the mineral bridge structures span the open fractures (Fig. 4d) (Laubach et al., 2004a; Lander and Laubach, 2015). The fractures exhibit macroscopic apertures and traces of hydrocarbon migration around the bridge structures (Fig. 4d). Microscope observation also reveals that fractures are partially filled with dolomite and siliceous. For the partially dolomite-filled fracture (Fig. 5c), its aperture ranges from 360.65 μm to 399.93 μm around the dolomite, gradually tapering down to 278.2 μm to 296 μm. As for the partially silicon-filled fractures (Fig. 5g), the aperture maintains a local aperture at 146.37 μm around siliceous cements. Accordingly, minerals spanning the open fractures can preserve the local effectiveness.

Fractures also undergo dissolution throughout deep burial (Tan et al., 2024). Effects of dissolution on fracture effectiveness are various. The dissolution of feldspar and rock fragment flanking the fracture surfaces enhance the local aperture by approximate 100 μm (Fig. 5a). When fractures are filled by soluble minerals such as calcite, subsequent dissolution causes the completely filled fractures to reopen. The aperture of new fracture ranges from 40 μm to 150 μm (Fig. 5h).

5.1.3 In-situ stress

The in-situ stress imposed on the Earth's crust rocks consists of structural stress, static rock stress, pore fluid pressure, and thermal stress (Narr and Currie, 1982). The stress state of Earth's crust rocks can be expressed by the maximum horizontal principal compressive stress (σ_H), the minimum principal horizontal compressive stress (σ_h), the vertical overburden stress (σ_V) (Fig. 10a). The three principal stress on the fracture surface can be further classified into shear stress (τ) and normal stress (σ_n) (Fig. 10a) (Ferrill et al., 2021). The σ_n is perpendicular to the fracture surface, and the τ is parallel to the fracture surface (Lu et al., 2018). The effective normal stress ($\sigma_{n'}$) on the fracture surface is related to the σn and pore pressure (P_p) (Feng, et al., 2020). Therefore, under the same differential stress, the $\sigma_{n'}$ is related to the angle (θ) between the fracture strike and the $D\sigma_H$. In general, the smaller the θ, the larger the $\sigma_{n'}$, the better the fracture effectiveness (Laubach et al., 2004a; Zeng et al., 2010; Liu et al., 2021; Lai et al., 2023b).

Based on rock magnetic fabric indications, tectonic stress field analysis, and borehole image logs, the $D\sigma_H$ in the Keshen gas field has always been the nearly N–S strike since the late Yanshan Stage (Zeng et al., 2004). Influenced by local faults and folds, the local $D\sigma_H$ can be altered. As a whole, the θ between the effective fracture strike and the $D\sigma_H$ exhibits a negative correlation with the effective fracture aperture (Fig. 10b). When the θ ranges from 0° to 30°, the aperture is between 47.13 μm and 154.87 μm, with an average aperture of 122.42 μm. Notably, certain effective fractures exhibit aperture exceeding 400μm, with a maximum reaching 788.44 μm. When the θ ranges from 30° to 60°, the aperture varies from 25.16μm to 104.75μm, maintaining an average aperture of 67.91 μm. When it comes to the θ ranging from 60° to 90°, the aperture ranges from 23.79 μm to 129.78 μm, with an average aperture of 119.34 μm (Fig. 10c). In addition, the average aperture corresponding to the θ between 60° and 90° surpasses that corresponding to the θ between 30° and 60°. Especially, it can be observed that three effective fractures exhibit apertures at 1923.01 μm, 1176.85 μm, and 1132.99 μm, with the θ 78.68°, 79.73°, and 80.6° in sequence. It can be inferred that these three fractures are the nearly E–W striking tensile fractures (Fig. 8b). Meanwhile, there may be minerals partially filling to counterbalance in-situ stress. Hence, the fracture effectiveness arises from the intricate interplay of various factors, with no single factor exerting decisive control.

During the 0–3 Ma period, influenced by intense tectonic compression and extensive natural gas charging, overpressure generally developed within the K_1bs (Guo et al., 2016). The maximum pressure coefficient exceeds 1.8 (Li et al., 2021). Overpressure can diminish the effective normal stress (Fig. 10a), and then change the stress state of the Earth's crust rocks. Influenced by this, shear fractures maybe develop (Zeng and Li, 2010). Simultaneously, overpressure can counterbalance the effective normal stress exerted on the fracture surface, and

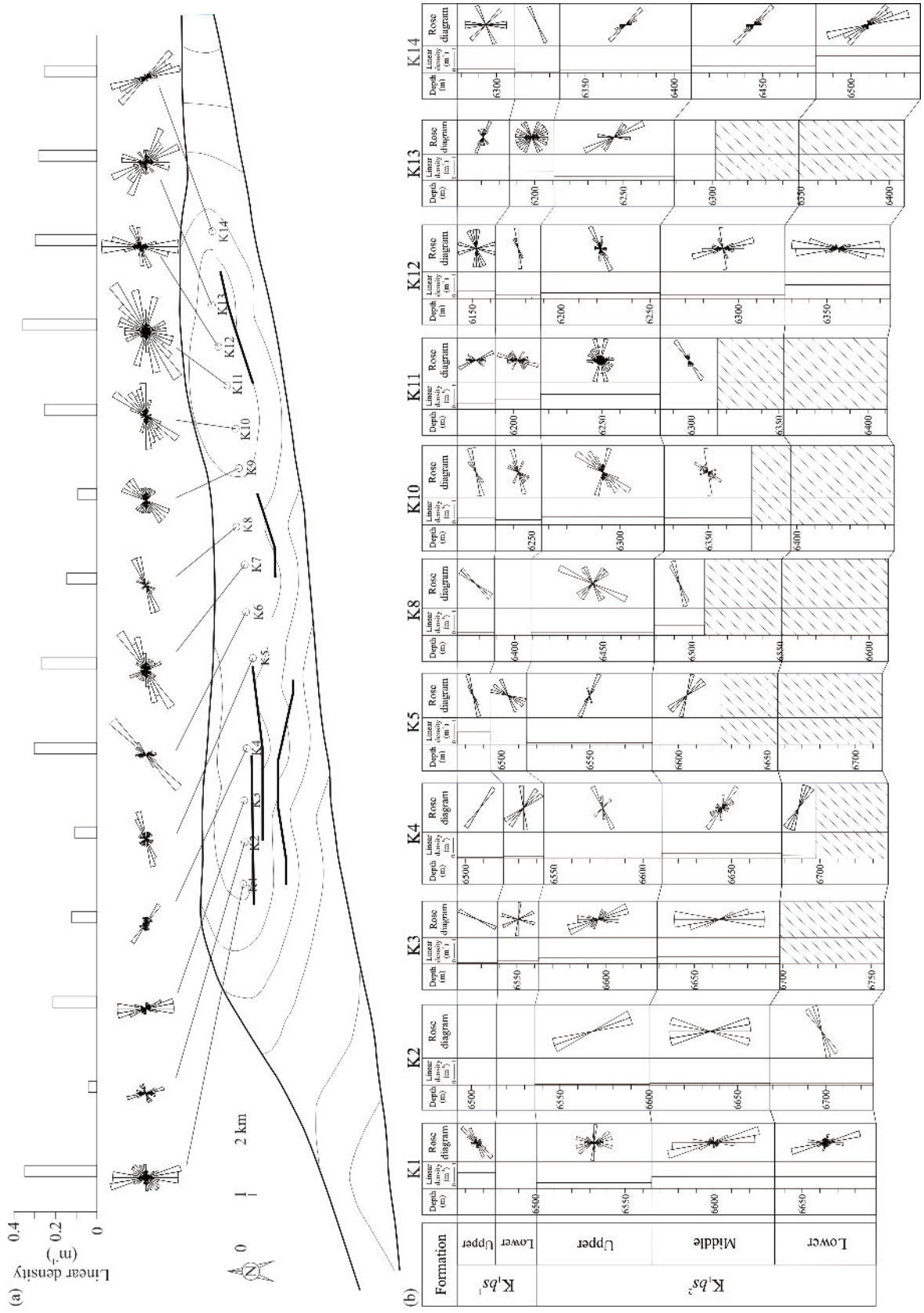

Fig. 7. Vertical and horizontal distribution laws of the linear density and strike of effective fractures.

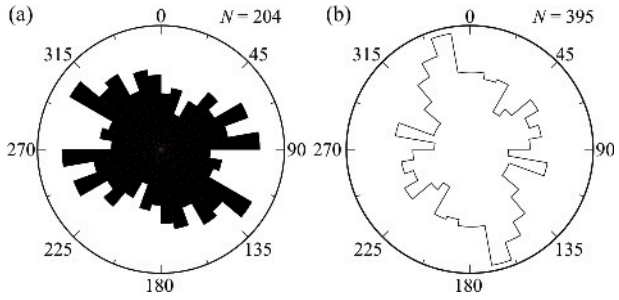

Fig. 8. Rose diagrams of ineffective fracture strike and effective fracture strike based on borehole image logs.
(a) Ineffective fractures (N = 204); (b) effective fractures (N = 395).

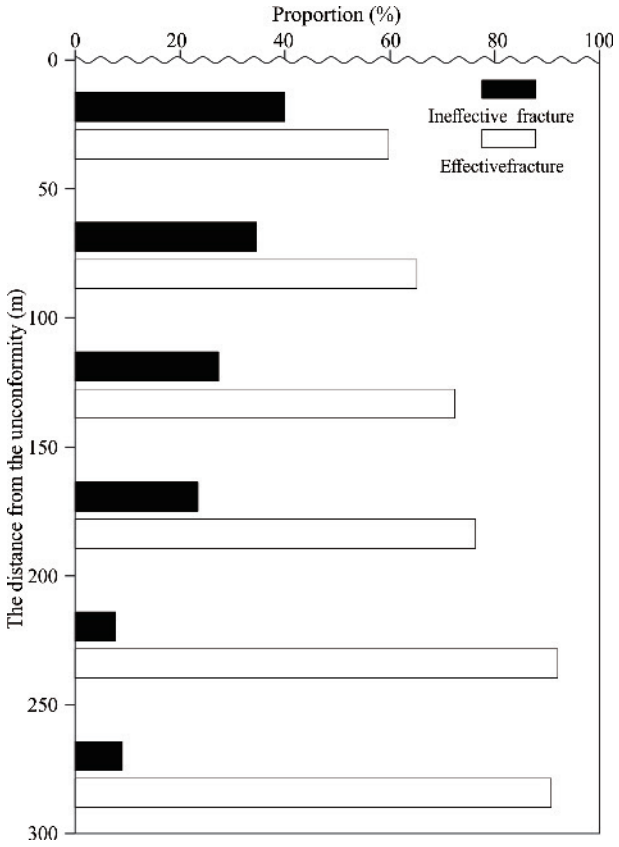

Fig. 9. Histogram of the proportion of ineffective/effective fractures at varying distances from the unconformity.

then preserve the fractures effectiveness. Additionally, when pore fluid pressure surpasses a certain threshold, the minimum principal stress undergoes a transition from compressive to tensile (Zeng and Li, 2010; Zeng et al., 2023b). This process can give rise to the formation of overpressure fractures (Fig. 4f).

However, with the continuous exploitation of gas reservoirs, the decreases in pore pressure can impact the fracture effectiveness (Becker et al., 2010). The double logarithmic curves of the pressure build-up test, the simulate pore fluid pressure and permeability for wells K2, K6, and K14 are shown in Fig. 11. For the same well, the pressure derivative curves exhibit a time-dependent decrease in concave amplitude. Simultaneously, the horizontal coordinate values corresponding to the pseudo-pressure curve show a time-dependent rise (Fig. 11a). The permeability exhibits a positive correlation with the pore fluid pressure (Fig. 11b). The P_p in well K2 decreased from 100.08 MPa to 82.55 MPa, resulting in a corresponding decrease in permeability from 15.66×10^{-3} μm^2 to 0.24×10^{-3} μm^2. The P_p of well K6 decreased from 99.93 MPa to 84.55 MPa, leading to a decrease in permeability from 125.07×10^{-3} μm^2 to 88.41×10^{-3} μm^2. Similarly, the P_p in well K14 experienced a decline from 100.38 MPa to 77.85 MPa, causing the permeability to decrease from 51.16×10^{-3}μm^2 to 34.99×10^{-3} μm^2. With a matrix permeability less than 0.1×10^{-3}μm^2 in the ultra-deep tight sandstone reservoir, its seepage capacity relies primarily on the effective fracture. Hence, the time-dependent sharp reductions in permeability indicate general declines in fracture effectiveness.

5.2 Effects of effective fractures on productivity

5.2.1 Productivity enhancement effects of effective fractures

Effective fractures can significantly enhance the permeability for ultra-deep tight sandstone reservoirs. Measured permeability of samples lacking fractures ranges from 0.001×10^{-3} μm^2 to 0.1×10^{-3} μm^2, while that of samples with fractures ranges from 0.1×10^{-3} μm^2 to 10×10^{-3} μm^2 (Fig. 12). Meanwhile, the permeability interpretated by well test can reach up to 125.0×10^{-3} μm^2 (Fig. 11). It can be inferred that effective fractures can enhance matrix permeability by several orders of magnitude, and then increase gas productivity.

For wells in eastern region, the linear density of effective fractures is positively correlated with the initial open flow potential, and their average aperture is similar (Fig. 13). Conversely, this relationship is poor for wells in western region. For example, for wells K2 and K4, there is a large difference in linear density of effective fractures, while the initial open flow potential is similar. The average apertures of effective fractures are 196.47 μm and 63.78 μm respectively (Fig. 13). Therefore, despite fewer effective fractures, the well K2 exhibits grander fracture aperture, and then show similar productivity with well K4. Meanwhile, for well K3, the average aperture of effective fractures is 120.98 μm and is lower than that in well K2. However, its linear density stands at 0.21 m^{-1} and far exceeds the 0.04 m^{-1} of well K2. Consequently, the difference in initial open flow potential between wells K2 and K3 remains relatively small. Therefore, the gas productivity is jointly influenced by the linear density and aperture of effective fractures.

Additionally, the initial open flow potential of well K1 exhibits very low, with a value of 20×10^4 m^3/d (Fig. 13). However, the linear density and average aperture of effective fractures are 0.35 m^{-1} and 242 μm respectively. These characteristics show a strong contradiction in gas production. In view of the production curve of well K1 (Fig. 15), at the beginning of exploitation, water invasion occurs immediately, with daily water production reach to 120 m^3/d. Hence, it can be inferred that intense water invasion results in the significant decreases in gas productivity.

As shown in Fig. 7, compared with the K_1bs^1, the linear

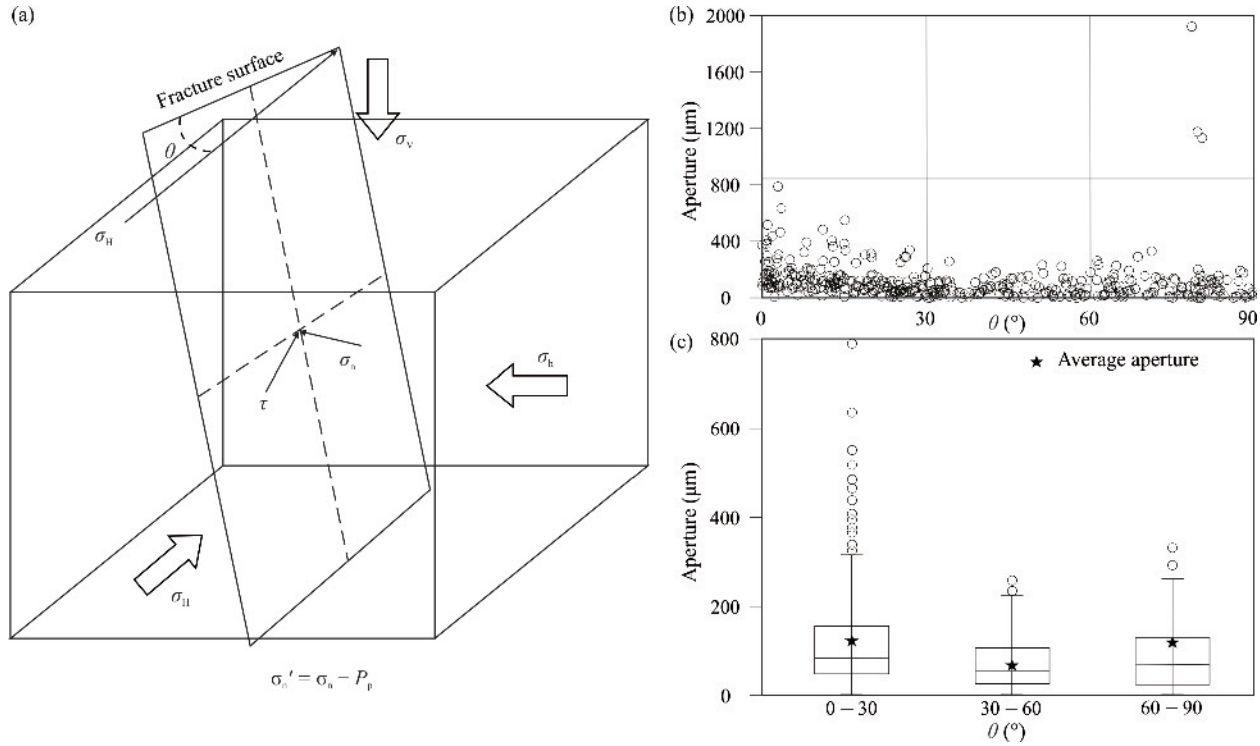

Fig. 10. (a) The stress state of the fracture surface (modified from Feng et al., 2020); (b) scatter plot of the relationship between the aperture and the θ; (c) Box diagram of the aperture corresponding to different angle intervals.

density of effective fractures exhibits more larger in the K_1bs^2. Based on gas production test for wells K1 and K6 (Fig. 14a), the gas production of the K_1bs^2 is higher than that of the K_1bs^1. Simultaneously, for well K1, due to completely filled fractures enrichment, certain perforating sections in the K_1bs^1 exhibit no gas production. Although ineffective fractures are completely filled with calcite (Fig. 6c), calcite is easily dissolved by acidic solutions. Hence, certain ineffective fractures can be transformed into effective fractures after acidizing. Taking well K6 as an example, gas production for different perforating sections exhibits various increase after acidizing. Especially for the 6448 m to 64456 m, ineffective fractures are activated, and gas production is restored (Fig. 14a). Besides, daily gas productions are all increased for different wells after acidification (Fig. 14b). Therefore, for fractures filled with soluble minerals, their effectiveness can be enhanced by acidification, and then play a key role on gas production.

5.2.2 Productivity reduction effects of effective fractures

With further exploitation of gas reservoirs, effective fractures may serve as rapid pathways for water invasion. When the effective fracture strike is parallel to the direction of water invasion, it can expedite water invasion. Conversely, it has the potential to impede water invasion. Meanwhile, the more abundant and the larger-scale the effective fractures, the severer water invasion is. At present, wells K1, K2, K3 are plagued by serious water invasion. The daily water production of wells K1 and K2 exceeds 600 m^3/d, while that of well K3 surpasses 200 m^3/d and well K4 reaches over 70 m^3/d (Fig. 15). Notably, the time-dependent variolations in daily water production exhibit strong heterogeneous water invasion for the four wells. Accordingly, the time-dependent variolations in daily gas production show strong heterogeneous. These characteristics all indicate the diverse development of effective fractures.

Based on the interwell pressure interference test and tracer monitoring, for wells K1 and K2, the pressure propagation velocity is 170 m/h, and the tracer migration velocity is 44.7 m/d. For wells K2 and K3, the pressure propagation velocity is 64.44 m/h (Fig. 16). Hence, there are high-speed migration pathways in the western region. However, the effective fractures in wells K1, K2 and K3 exhibit the nearly N–S strikes. They are nearly perpendicular to the orientation of pressure propagation and tracer migration. Obviously, this pattern poses challenges for fluid migration. However, the structural plan exhibits that two nearly E–W striking faults are in the western region (Fig. 16). It is inferred that the two faults act as high-speed migration pathways. The macroscopic water invasion pattern exhibits that formation water invades along the fault and then permeates through the effective fractures (Fig. 16). Accordingly, for the wells K1, K2, and K3, the nearly N–S striking effective fractures can expedite water invasion (Fig. 16). Conversely, for the well K4, the NW–SE striking effective fractures can imped water invasion (Fig. 16). Meanwhile, as formation water gradually invades the eastern region, the NEE–SWW and nearly E–W striking effective fractures also expedite water invasion, and then decrease gas productivity (Fig. 16).

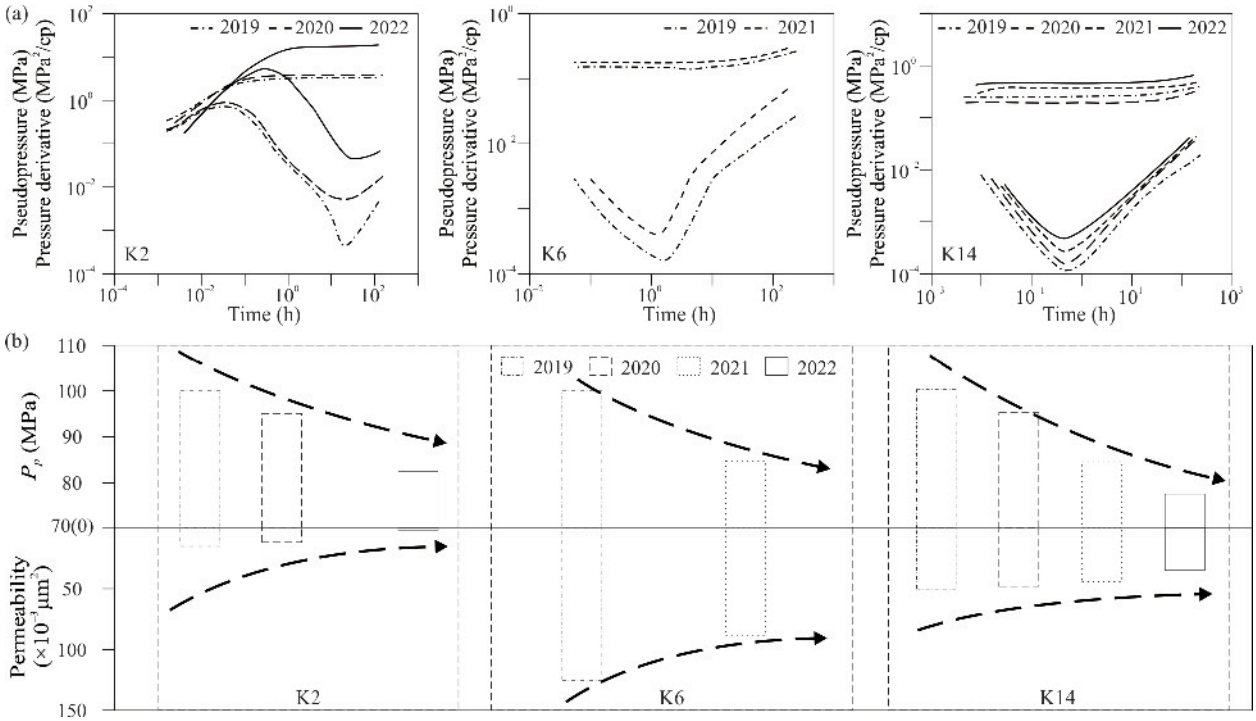

Fig. 11. (a) Double logarithmic curves of the pressure build-up test for wells K2, K6 and K14; (b) histogram of time-dependent *Pp* and permeability interpretated by well test for wells K2, K6 and K14.

Based on the aperture of effective fractures of wells K1, K2, K3, and K4, they exhibit a multi-scale characteristic. Consequently, this study categorizes I-fracture as those with an aperture exceeding 1000μm, classifies II-fracture as having an aperture ranging from 100 μm to 1000 μm, and designates III-fracture as possessing an aperture between 10 μm and 100 μm (Fig. 17). Based on the linear density, aperture, and strike of effective fractures and the production curves (Figs. 15–17), the heterogeneous variations in gas productivity are analyzed. For well K1, it exhibits major development of II-fractures, accompanied by the presence of I-fractures. These fractures are nearly parallel to the later water invasion orientation. Therefore, the water invasion swiftly traverses along these fractures, leading to a precipitous decline in gas production (Fig. 15a). As for well K2, it exhibits a relatively development of II-fractures, accompanied by a limited number of III-fractures. The effective fractures are nearly parallel to the later water invasion orientation. The formation water relatively swiftly permeates through the fracture network. The gas productivity remains stable during the initial stage of production. As water invasion occurs, it can maintain short-term production. Subsequently, there is an abrupt decline in gas productivity (Fig. 15b). The well K3 develops II–III-fractures, with sporadic approximate I-fracture. The effective fractures are also nearly parallel to the later water invasion orientation. The formation water relatively rapidly penetrates along the fracture network. The gas productivity can long-term maintain stability. Accompanied with water invasion, the gas production rapidly decreases (Fig. 15c). The well K4 predominantly exhibits III-fractures. The effective fracture strike is nearly perpendicular to the water invasion orientation. The formation water slowly penetrates along the fracture network. Accordingly, the gas productivity can maintain long-term stability before and after water invasion (Fig. 15d). Therefore, the linear density, aperture and strike of effective fractures are crucial factors on water invasion, thereby resulting in reduction in gas productivity.

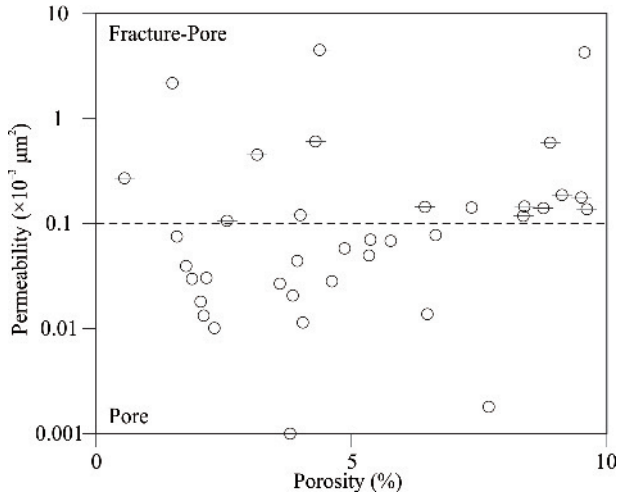

Fig. 12. The scatter plot of the measured porosity and permeability.

Based on the development characteristics of effective fractures, certain policies can be put forward for efficient exploitation. In the initial stage of exploitation, with abundant effective fractures in the K_1bs^2, it can be preferential selection for perforation. As P_p decreases with

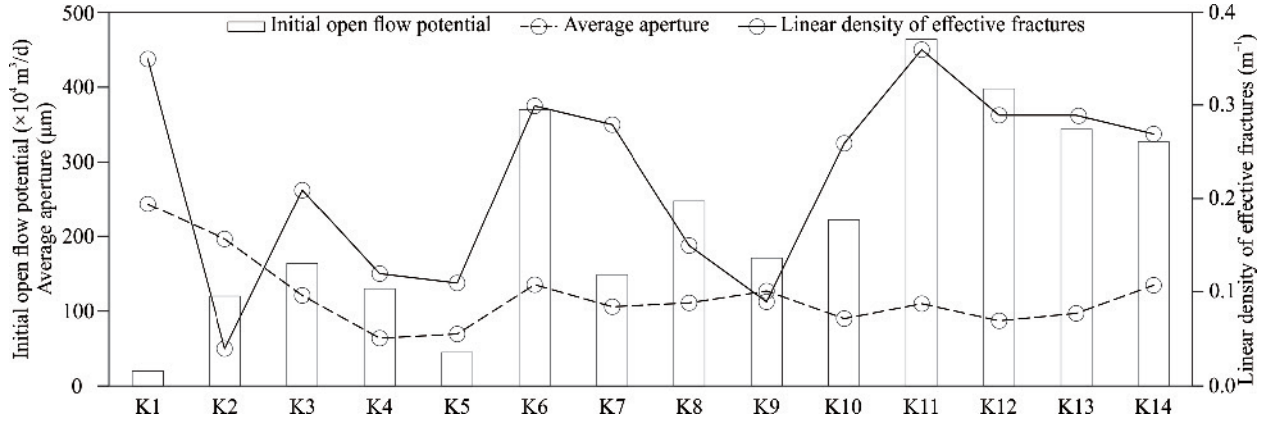

Fig. 13. Line charts of the linear density and average aperture of effective fractures for different gas wells, and the histogram of the initial open flow potential for different gas wells.

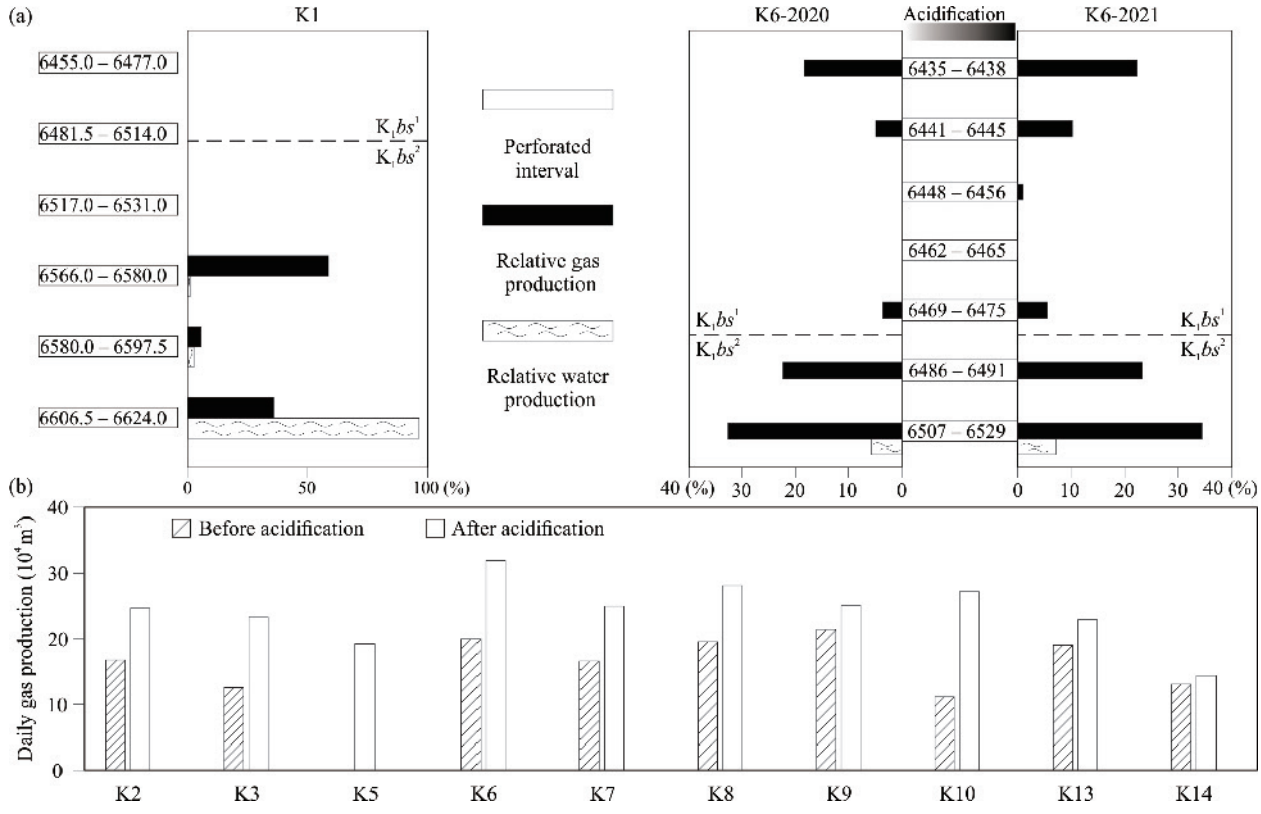

Fig. 14. (a) The gas production test for wells K1 and K6; (b) the histogram of daily gas production before and after acidification for different wells.

exploitation, measures such as acidification and fracturing can be implemented to activate ineffective fractures, and then enhance gas productivity. Influenced by intense water invasion, the western region exhibits extremely low gas productivity. To delay water invasion in the eastern region, drainage wells between well K4 and well K5 can be deployed. Gas productivity tests show that the lower K_1bs^2 constitutes the primary aquifer (Fig. 14a). The effective fractures predominantly exhibit the NWW–SEE and NEE–SWW strike. Therefore, the N–S striking horizontal or high deviated wells can be deployed within the middle–lower K_1bs^2. In this way, most effective fractures can be cut off to achieve water prevention and control, and then gas productivity can be maintained in the eastern region.

6 Conclusions

Nature fractures can be classified into tectonic fracture, diagenetic fracture (bedding fracture), and overpressure fracture. Tectonic fracture is the primary type. Tectonic fractures are mainly high-angle and vertical shear fractures, followed by tensile fracture. Most fractures are completely filled and primarily filled by calcite. Tectonic fractures exhibit the nearly N–S, NEE–SWW, NWW–SEE

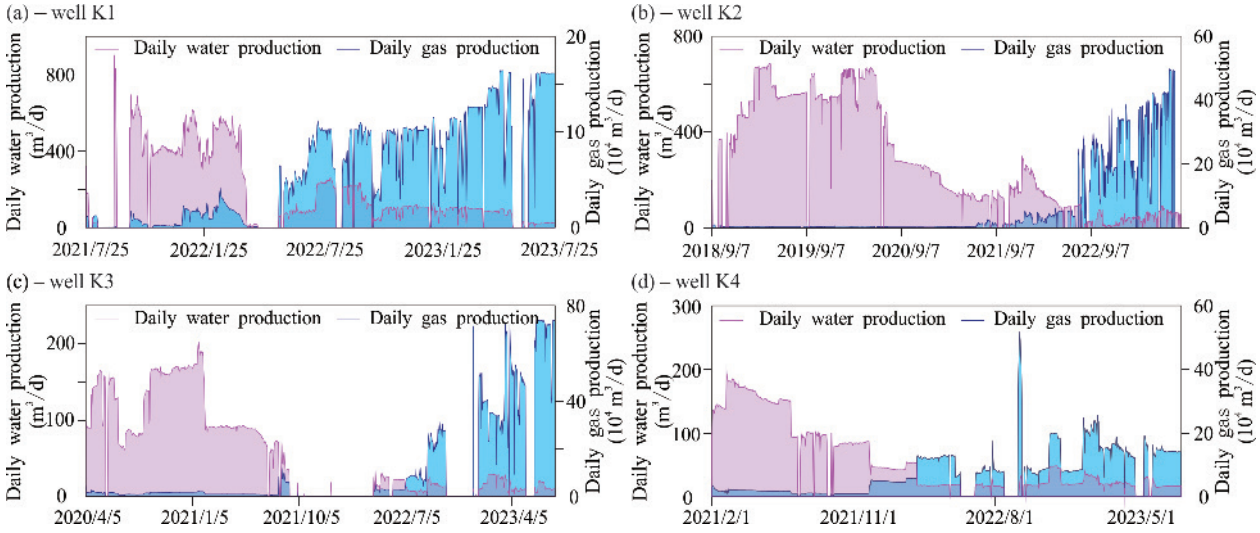

Fig. 15. The daily gas and water production curves of wells K1, K2, K3, and K4.

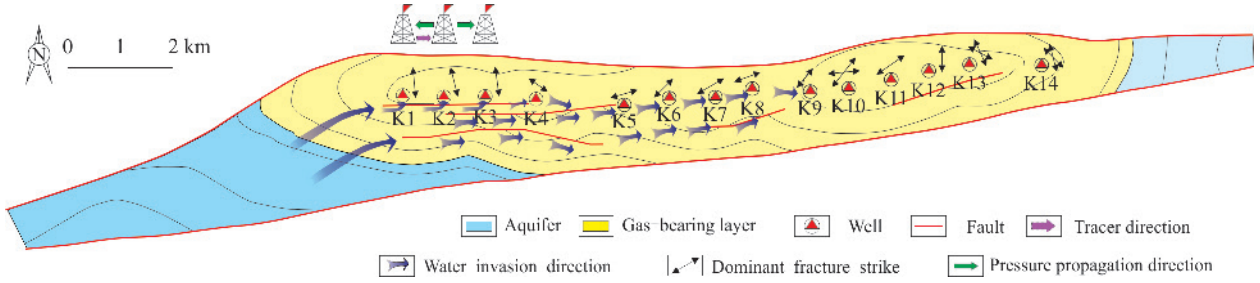

Fig. 16. The macroscopic water invasion pattern of the gas reservoir.

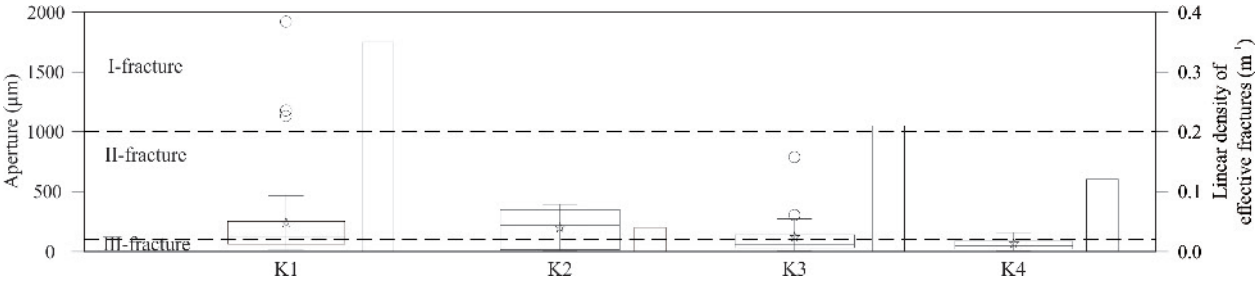

Fig. 17. The box diagram of the aperture of effective fractures and the histogram of the linear density of effective fractures in wells K1, K2, K3, and K4.

and nearly E–W strikes.

Horizontally, the eastern region is abundance of effective fractures and exhibits high gas productivity. In contrast, the western region shows the presence of faults and large-scale fractures, and influenced by intense water invasion. Within the western region, effective fractures exhibit the nearly N–S strike, while gradually transition towards the NW–SE strike. Within the eastern region, there is a gradual shift from the NEE–SWW strike to the NNE–SSW strike and subsequently to the NNW-SSE strike. Vertically, the middle-lower K_1bs^2 is abundant in effective fractures and exhibits high gas productivity. Overall, effective fractures exhibit the nearly E–W and NEE–SWW strikes within K_1bs^1, and transformed to the nearly N–S and NNW–SSE strikes within K_1bs^2.

Tectonism, diagenesis and in-situ stress are primary factors on fracture effectiveness. Fractures formed by earlier tectonic movements are more prone to being filled due to long-term diagenesis. Completely filled fractures can be reopened by the later tectonic movement. The injection of fluids from the gypsum rock results in high filling rate of adjacent fractures. Overgrowths of quartz and albite flanking the fracture surfaces lead to the reduction of local fracture aperture. Minerals spanning the fracture surfaces can preserve the local fracture effectiveness from the later tectonic compression. Effectiveness of the fracture filled by soluble minerals can be enhanced by acidization. The smaller the angle between the effective fracture strike and the $D\sigma_H$, the better the fracture effectiveness. Overpressure can effectively decrease the effective normal stress on the fracture surfaces. However, with the further exploitation, the

reduction of pore pressure decreases the fracture effectiveness.

The linear density, aperture, and strike of effective fractures are crucial factors on gas productivity. Effective fractures can enhance matrix permeability by several orders of magnitude. The more abundant and the larger-scale the effective fractures, the higher the gas productivity. With further exploitation, effective fractures act as high-speed pathways for water invasion. Influenced by intense water invasion, the gas productivity exhibits rapid decline. Especially, when the effective fracture strike is parallel to the water invasion orientation, it can accelerate gas productivity decline.

Acknowledgments

This article is supported by the National Natural Science Foundation of China (No. U21B2062). The author highly appreciates the data and support from the Exploration and Development Research Institute of Tarim Oilfield Company, PetroChina. Thank the editor and several anonymous reviewers for their constructive comments, which have significantly contributed to the improvement of this article.

Manuscript received Mar. 27, 2024
accepted Jul. 24, 2024
associate EIC: ZHANG Shuichang
edited by FEI Hongcai

References

Aghli, G., Moussavi-Harami, R., and Mohammadian, R., 2020. Reservoir heterogeneity and fracture parameter determination using electrical image logs and petrophysical data (A case study, carbonate Asmari Formation, Zagros Basin, SW Iran). Petroleum Science, 17(1): 51–69.

Becker, S.P., Eichhubl, P., Laubach, S.E., Reed, R.M., Lander, R.H., and Bodnar, R.J., 2010. A 48 m.y. history of fracture opening, temperature, and fluid pressure: Cretaceous Travis Peak Formation, East Texas basin. Geological Society of America Bulletin, 122(7–8): 1081–1093.

Bjørlykke, K., 2014. Relationships between depositional environments, burial history and rock properties: Some principal aspects of diagenetic process in sedimentary basins. Sedimentary Geology, 301: 1–14.

Bloch, S., Lander, R. H., and Bonnell, L., 2002. Anomalously high porosity and permeability in deeply buried sandstone reservoirs: Origin and predictability. AAPG Bulletin, 86(2): 301–328.

Bons, P.D., Elburg, M.A., and Gomez-Rivas, E., 2012. A review of the formation of tectonic veins and their microstructures. Journal of Structural Geology, 43: 33–62.

Cao, B.F., Luo, X.R., Zhang, L.K., Sui, F.G., Lin, H.X., and Lei, Y.H., 2017. Diagenetic evolution of deep sandstones and multiple-stage oil entrapment: A case study from the Lower Jurassic Sangonghe Formation in the Fukang Sag, central Junggar basin (NW China). Journal of Petroleum Science and Engineering, 152: 136–155.

Cao, B.F., Luo, X.R., Zhang, L.K., Lei, Y.H., and Zhou, J.S., 2020. Petrofacies prediction and 3-D geological model in tight gas sandstone reservoirs by integration of well logs and geostatistical modeling. Marine and Petroleum Geology, 114: 104202.

Cao, B.F., Sun, W., and Li, J., 2021. Reservoir petrofacies-A tool for characterization of reservoir quality and pore structures in a tight sandstone reservoir: A study from the sixth member of Upper Triassic Yanchang Formation, Ordos Basin, China. Journal of Petroleum Science and Engineering, 199: 108294.

Cao, B.F., Luo, X.R., Wang, X., Zhang, L.Q., Shi, H., 2023. Calcite-cemented concretions in non-marine sandstones: An integrated study of outcrop sedimentology, petrography and clumped isotopes. Sedimentology, 70(4): 1039–1074.

Cao, B.F., Luo, X.R., Worden, R.H., Wang, X.Z., He, Y.H., Qiao, X.Y., Zhang, L.K., Lei, Y.H., Zhou, J.S., Deng, C., 2024. Contrasting diagenetic evolution and hydrocarbon charge of tight gas sandstones in the lower Permian Shanxi Formation, southeastern Ordos Basin, China. Journal of Asian Earth Science, 276: 106330.

Cao, D.S., Zeng, L.B., Gomez-Rivas, E., Gong, L., Liu, G.P., Lu, G.Q., Bons, P.D., 2024. Correction of linear fracture density and error analysis using underground borehole data. Journal of Structural Geology, 184: 105152.

Cao, Y.C., Yuan, G.H., Yang, H.J., Wang, Y.Z., Liu, K.Y., Zan, N.M., Xi, K.L., and Wang, J., 2022. Current situation of oil and gas exploration and research of the origin of high-quality reservoirs in deep-ultra-deep clastic reservoirs of petroliferous basins. Acta Petrolei Sinica, 43(1): 112–140 (in Chinese with English abstract).

Chatterjee, S., and Mukherjee, S., 2023. Review on drilling-induced fractures in drill cores. Marine and Petroleum Geology, 151: 106089.

Cobbold, P.R., Zanella, A., Rodrigues, N., and Løseth, H., 2013. Bedding-parallel fibrous veins (beef and cone-in-cone): Worldwide occurrence and possible significance in terms of fluid overpressure, hydrocarbon generation and mineralization. Marine and Petroleum Geology, 43: 1–20.

Du, X.Y., Jin, Z.J., Zeng, L.B., Liu, G.P., He, W.J., Ostadhassan, M., Song, Y., Liang, X.P., Yang, S., and Lu, G.Q., 2023. Formation of natural fractures and their impact on shale oil accumulation in the Mahu sag, Junggar Basin, NW China. International Journal of Coal Geology, 279: 104385.

Feng, J.W., Shi, S., Zhou, Z.H., Li, X.Z., and Luo, P., 2019. Characterizing the influence of interlayers on the development and distribution of fractures in deep tight sandstones using finite element method. Journal of Structural Geology, 123: 81–95.

Feng, J.W., Zhao, L.B., and Wang, Y.D., 2020. Controlling factors for productivity of ultra-deep tight reservoirs in Keshen gas field, Kuqa depression. Acta Petrolei Sinica, 41 (4): 478–488 (in Chinese with English abstract).

Ferrill, D.A., Smart, K.J., Cawood, A.J., and Morris, A.P., 2021. The fold-thrust belt stress cycle: Superposition of normal, strike-slip, and thrust faulting deformation regimes. Journal of Structural Geology, 148: 104362.

Gale, J.F.W., Lander, R.H., Reed, R.M., and Laubach, S.E., 2010. Modeling fracture porosity evolution in dolostone. Journal of Structural Geology, 32(9): 1201–1211.

Gong, L., Zeng, L.B., Du, Y.J., and Han, Z.R., 2015. Influence of structural diagenesis on fracture effectiveness: A case study of the Cretaceous tight sandstone reservoirs of Kuqa foreland basin. Journal of China University of Mining & Technology, 44(3): 514–519 (in Chinese with English abstract).

Gong, L., Gao, M.Z., Zeng, L.B., Fu, X.F., Gao, Z.Y., Gao, A., Zu, K.W., and Yao, J.Q., 2017. Controlling factors on fracture development in the tight sandstone reservoirs: A case study of Jurassic–Neogene in the Kuqa foreland basin. Natural Gas Geoscience, 28(2): 199–208 (in Chinese with English abstract).

Guo, X.W., Liu, K.Y., Jia, C.Z., Song, Y., Zhao, M.J., Zhuo, Q.G., and Lu, X.S., 2016. Constraining tectonic compression processes by reservoir pressure evolution: Overpressure generation and evolution in the Kelasu thrust belt of Kuqa foreland basin, NW China. Marine and Petroleum Geology, 72: 30–44.

He, D.F., 2022. Mutil-cycle superimposed sedimentary basins in China: Formation, evolution, geologic, framework and hydrocarbon occurrence. Earth Science Frontiers, 29(6): 24–59 (in Chinese with English abstract).

Hudec, M.R., and Jackson, M.P.A., 2007. Terra infirma: Understanding salt tectonics. Earth-Science Reviews, 82(1–2): 1–28.

Jia, A.L., Tang, H.F., Han, Y.X., Lü, Z.K., Liu, Q.M., Zhang, Y.Z., Sun, H.D., Huang, W.G., and Wang, Z.L., 2019. The distribution of gas and water and development strategy for

deep-buried gasfield in Kuqa depression, Tarim basin. Natural Gas Geoscience, 30(6): 90–918 (in Chinese with English abstract).

Jia, C.Z., 2023. Key scientific and technological problems of petroleum exploration and development in deep and ultra-deep formation. Journal of China University of Petroleum (Edition of Natural Science), 47(5): 1–12 (in Chinese with English abstract).

Jia, C.Z., Zheng, M., and Zhang, Y.F., 2012. Unconventional hydrocarbon resources in China and the prospect of exploration and development. Petroleum Exploration and Development, 39(2): 139–146.

Lai, J., Wang, G.W., Fan, Z.Y., Wang, Z.Y., Chen, J., Zhou, Z.L., Wang, S.C., and Xiao, C.W., 2017. Fracture detection in oil-based drilling mud using a combination of borehole image and sonic logs. Marine and Petroleum Geology, 84: 195–241.

Lai, J., Bai, T.Y., Li, H.B., Pang, X.J., Bao, M., Wang, G.W., Liu, B.C., and Liu, S.C., 2023a. Geological and engineering sweet spots in the Permian Lucaogou formation, Jimisar sag, Junggar basin. Acta Geologica Sinica (English Edition), 97 (4): 1214–1228.

Lai, J., Li, D., Bai, T.Y., Zhao, F., Ai, Y., Liu, H.K., Cai, D.Y., Wang, G.W., Chen, K.J., and Xie, Y.Q., 2023b. Reservoir quality evaluation and prediction in ultra-deep tight sandstones in the Kuqa depression, China. Journal of Structural Geology, 170: 104850.

Lander, R.H., and Laubach, S.E., 2015. Insights into rates of fracture growth and sealing from a model for quartz cementation in fractured sandstones. Geological Society of America Bulletin, 127(3–4): 516–538.

Laubach, S.E., 2003. Practical approaches to identifying sealed and open fractures. AAPG Bulletin, 87(4): 561-579.

Laubach, S.E., and Ward, M.E., 2006. Diagenesis in porosity evolution of opening-mode fractures, Middle Triassic to Lower Jurassic La Boca Formation, NE Mexico. Tectonophysics, 419(1–4): 75–97.

Laubach, S.E., Olson, J.E., and Gale, J.F.W., 2004a. Are open fractures necessarily aligned with maximum horizontal stress? Earth and Planetary Science Letters, 222(1): 191–195.

Laubach, S.E., Reed, R.M., Olson, J.E., Lander, R.H., and Bonnell, L.M., 2004b. Coevolution of crack-seal texture and fracture porosity in sedimentary rocks: Cathodoluminescence observations of regional fractures. Journal of Structural Geology, 26(5): 967–982.

Laubach, S.E., Olson, J.E., and Gross, M.R., 2009. Mechanical and fracture stratigraphy. AAPG Bulletin, 93 (11): 1413–1426.

Laubach, S.E., Eichhubl, P., Hilgers, C., and Lander, R.H., 2010. Structural diagenesis. Journal of Structural Geology, 32(12): 1866–1872.

Laubach, S.E., Fall, A., Copley, L.K., Marrett, R., and Wilkins, S.J., 2016. Fracture porosity creation and persistence in a basement-involved Laramide fold, upper Cretaceous Frontier Formation, Green River Basin, USA. Geological Magazine, 153(5–6): 887–910.

Laubach, S.E., Lander, R.H., Criscenti, L.J., Anovitz, L.M., Urai, J.L., Pollyea, R.M., Hooker, J.N., Narr, W., Evans, M.A., Kerisit, S.N., Olson, J.E., Dewers, T., Fisher, D., Bodnar, R., Evans, B., Dove, P., Bonnell, L.M., Marder, M.P., and Pyrak-Nolte, L., 2019. The role of chemistry in fracture pattern development and opportunities to advance interpretations of geological materials. Reviews of Geophysics, 57(3): 1065–1111.

Li, J., Zhang, C.M., Xiao, C.W., Li, J.F., and Yuan, S.J., 2008. Quantitative evalution method of fracturing sandstone reservoir and its application in Kuqa area, the Tarim basin. Natural Gas Industry, 28(10): 25–27 (in Chinese with English abstract).

Li, W., Chen, Z.X., Huang, P.H., Yu, Z.C., Min, L., and Lu, X.S., 2021. Formation of overpressure system and its relationship with the distribution of large gas field in typical foreland basins in central and western China. Petroleum Exploration and Development, 48(3): 625–640.

Li, Y., Guo, S., Wang, X., Hou, Y.F., Neng, Y., Wang, Z.X., Zhou, L., Yang, W.J., and Tan, C., 2017. Stratification model of an ultra-deep tight sandstone fracture reservoir under tectonic stress: A case study of a Cretaceous reservoir in the Kuqa foreland thrust belt of the Tarim basin. Journal of Natural Gas Science and Engineering, 45: 53–64.

Liu, G.P., Zeng, L.B., Zhu, R.K., Gong, L., Ostadhassan, M., and Mao, Z., 2021. Effective fractures and their contribution to the reservoirs in deep tight sandstones in the Kuqa Depression, Tarim basin, China. Marine and Petroleum Geology, 124: 104824.

Liu, G.P., Jin, Z.J., Zeng, L.B., Huang, L.L., Ostadhassan, M., Du, X.Y., Lu, G.Q., and Zhang, Y.Z., 2023. Natural fractures in deep continental shale oil reservoirs: A case study from the Permian Lucaogou formation in the Eastern Junggar basin, Northern China. Journal of Structural Geology, 174: 104913.

Liu, Q.M., Tang, H.F., Lü, Z.K., Wang, Q.F., Liu, Z.L., and Chang, B.H., 2023. Study on gas-water distribution and water invasion law under different fracture development models in ultra-deep gas reservoir: Taking Keshen 2, 9 and 8 gas reservoirs of Tarim basin as examples. Natural Gas Geoscience, 34(6): 963–972 (in Chinese with English abstract).

Lu, Y.L., Lü, H.Z., Cui, Y.J., and Chen, H.B., 2018. Method for fracture effectiveness evaluation based on 3D Mohr Circle and its application. Acta Petrolei Sinica, 39(5): 564–569 (in Chinese with English abstract).

Lü, Z.K., Tang, H.F., Liu, Q.M., Tang, Y.L., Wang, Q.F., Chang, B.H., and Nie, Y.B., 2022. Dynamic evaluation method of water sealed gas for ultra-deep fractured tight gas reservoir in Kuqa Depression, Tarim basin. Natural Gas Geoscience, 33 (11): 1874 –1882 (in Chinese with English abstract).

Lyu, W.Y., Zeng, L.B., Lyu, P., Yi, T., Dong, S.Q., Wang, S.J., Xu, X., and Chen, H., 2022. Insights into the mechanical stratigraphy and vertical fracture patterns in tight oil sandstones: The upper Triassic Yanchang Formation in the eastern Ordos basin, China. Journal of Petroleum Science and Engineering, 212: 110247.

Narr, W., and Currie, J.B., 1982. Origin of fracture porosity: Example from Altament Field, Utah. AAPG Bulletin, 66(9): 1231–1247.

Nelson, R.A., 2001. Geologic analysis of naturally fractured reservoirs. Gulf Professional, Houston.

Qi, J.F., Li, Y., Xu, Z.P., Yang, S.J., and Sun, T., 2023. A structural interpretation model and restoration of the Mesozoic proto-basin for the Kuqa depression, Tarim basin. Acta Geologica Sinica (English Edition), 97(1): 207–225.

Rashid, F., Hussein, D., Lorinczi, P., and Glover, P.W.J., 2023. The effect of fracturing on permeability in carbonate reservoir rocks. Marine and Petroleum Geology, 152: 106240.

Shen, Y.Q., Lü, X.X., Guo, S., Song, X., and Zhao, J., 2017. Effective evaluation of gas migration in deep and ultra-deep tight sandstone reservoirs of Keshen structural belt, Kuqa depression. Journal of Natural Gas Science and Engineering, 46: 119–131.

Sun, S., Hou, G.T., and Zheng, C.F., 2018. Prediction of tensile fractures in KS2 trap, Kuqa depression, NW China. Marine and Petroleum Geology, 101: 108–116.

Tan, X.L., Zeng, L.B., She, M., Li, H., Mao, Z., Song, Y.C., Yao, Y.T., Wang, J.P., and Lü, Y.Z., 2024. Impact of burial dissolution on the development of ultra-deep fault-controlled carbonate reservoirs: Insights from high-temperature and high-pressure dissolution kinetic simulation. Acta Geologica Sinica (English Edition). https://doi.org/10.1111/1755-6724.15166.

Wang, J.P., Zhang, H.L., Zhang, R.H., Yang, X.J., Zeng, Q.L., Chen, X.G., and Zhao, J.Q., 2018. Enhancement of ultra-deep tight sandstone reservoir quality by fractures: A case study of Keshen gas field in Kuqa depression, Tarim Basin. Oil & Gas Geology, 39(1): 77–88 (in Chinese with English abstract).

Wang, J.P., Zeng, L.B., Yang, X.Z., Liu, C., Wang, K., Zhang, R.H., Chen, X.G., Qu, Y.J., Laubach, S.E., and Wang, Q.Q., 2021. Fold-related fracture distribution in Neogene, Triassic, and Jurassic sandstone outcrops, northern margin of the Tarim basin, China: Guides to deformation in ultra-deep tight sandstone reservoirs. Lithosphere, (Special 1): 8330561.

Wang, J.P., Yang, X.Z., Zhang, J., Wang, K., Zhang, R.H., Wang, Q.Q., Ren, B., and Ukar, E., 2023a. Subsurface fracture characterization in a folded ultra-deep tight-gas sandstone

reservoir: A case study from the Keshen gas field, Tarim basin, China. Journal of Structural Geology, 172: 104867.
Wang, J.P., Zeng, L.B., Zhou, L., Wang, K., Zeng, Q.L., Zhang, Z.Y., Zhang, R.H., and Ma, X.W., 2023b. Development model of natural fractures in ultra-deep sandstone reservoirs with low porosity in Kelasu tectonic belt, Tarim basin. Earth Science, 48(7): 2520–2534 (in Chinese with English abstract).
Wang, K., Yang, H.J., Li, Y., Zhang, R.H., Yang, X.J., and Wang, J.P., 2020. Formation sequence and distribution of structural fractures in compact sandstone reservoir of Keshen gas field in Kuqa depression, Tarim basin. Geotectonica et Metallogenia, 44(1): 30–46 (in Chinese with English abstract).
Wang, Y., Wang, J., Zhao, W., Ji, P., Cheng, S., and Yu, H., 2023. Explicit original gas in place determination of naturally fractured reservoirs in gas well rate decline analysis. Advances in Geo-Energy Research, 2023, 9(2): 117–124.
Wang, Z., Lü, X.X., Wang, S., Li, Y., Zhou, X.X., Quan, H., and Li, R.B., 2020. Fracture systems and petrophysical properties of tight sandstone undergoing regional folding: A case study of the Cretaceous reservoirs in the Kuqa foreland thrust belt, Tarim Basin. Marine and Petroleum Geology, 112: 104055.
Wei, C., Zhang, C.Z., Chen, D., Sun, X.W., Liu, L., and Li, S.L., 2019. Seepage characteristics and development mechanism characterized by faults-fracture-pores "triple medium" in Keshen 2 gas reservoirs, Tarim basin. Natural Gas Geoscience, 30(12): 1684–1693 (in Chinese with English abstract).
Wei, G.Q., Wang, J.P., Zeng, L.B., Tang, Y.L., Wang, K., Liu, T.T., and Yang, Y., 2020. Structural reworking effects and new exploration discoveries of subsalt ultra-deep reservoirs in the Kelasu tectonic zone. Natural Gas Industry, 40(1): 20–30 (in Chinese with English abstract).
Xia, L., Xi, K.L., Yang, X.Z., Han, Z.H., Xu, Z.P., Zhou, L., Yu, G.D., Wang, D.S., and Wang, W.Y., 2024. Relationship between natural fractural fracture and structural style and its implication for tight gas enrichment: A case study of deep Ahe formation in the Dibei–Tuzi area, Kuqa depression. Acta Geologica Sinica (English Edition), 98(4): 1086–1110.
Xu, X.T., Zhang, L.K., Zeng, L.B., Li, C., Zhang, L.Q., Zeng, Z.P., and Ren, X.C., 2023. Effects of overpressure on deep sandstone reservoir quality: A case study of the Medium and Lower Jurassic formation in the Shawan sag, central Junggar Basin, Western China. Geoenergy Science and Engineering, 230: 212203.
Yang, L.L., Li, X.W., Zhuo, Q.G., Yu, Z.C., Yang, Y.L., and Liu, K.Y., 2022. Effects of gypsum–salt rock on mineral transformations in a saline lacustrine basin: Significance to reservoir development. Journal of Petroleum Science and Engineering, 211: 110240.
Zeng, L.B., and Li, Y.G., 2010. Tectonic fractures in tight gas sandstones of the upper Triassic Xujiahe Formation in the western Sichuan basin, China. Acta Geologica Sinica (English Edition), 84(5): 1229–1238.
Zeng, L.B., Tan, C.X., and Zhang, M.L., 2004. Tectonic stress field and its effect on hydrocarbon migration and accumulation in Mesozoic and Cenozoic in Kuqa depression. Tarim basin. Science in China (Series D: Earth Science), 34 (Supp. I): 98–106 (in Chinese with English abstract).
Zeng, L.B., WANG, H.J., Gong, L., and Liu, B.M., 2010. Impacts of the tectonic stress field on natural gas migration and accumulation: a case study of the Kuqa Depression in the Tarim Basin, China. Marine and Petroleum Geology, 27(7): 1616–1627.
Zeng, L.B., Zhu, R.K., Gao, Z.Y., Gong, L., and Liu, G.P., 2016. Structural diagenesis and its petroleum geological significance. Petroleum Science Bulletin, 1(2): 191–197 (in Chinese with English abstract).
Zeng, L.B., Lyu, W.Y., Li, J., Guo, Y.C., Yang, Y., Dong, S.Q., Liu, X.Z., and Zu, K.W., 2019. Variation in the orientation of the maximum horizontal stress in thick channel-fill sandstones with low-permeability: A case of the Bonan Oilfield in the Bohai Bay Basin, Eastern China. Marine and Petroleum Geology, 107: 32–40.
Zeng, L.B., Gong, L., Guan, C., Zhang, B.J., Wang, Q.Q., Zeng, Q., and Lyu, W.Y., 2022. Natural fractures and their contribution to tight gas conglomerate reservoirs: A case study in the northwestern Sichuan Basin, China. Journal of Petroleum Science and Engineering, 210: 110028.
Zeng, L.B., Gong, L., Zhang, Y.Z., Dong, S.Q., and Lyu, W.Y., 2023a. A review of the genesis, evolution, and prediction of natural fractures in deep tight sandstones of China. AAPG Bulletin, 107(10): 1687–1721.
Zeng, L.B., Song, Y.C., Liu, G.P., Tan, X.L., Xu, X.T, Yao, Y.T., and Mao, Z., 2023b. Natural fractures in ultra-deep reservoirs of China: A review. Journal of Structural Geology, 175: 104954.
Zeng, L.B., Mao, Z., Liu, G.P., Tian, H., Yao, Y.T., Zu, K.W., Dong, S.Q., and Ostadhassan, M., 2024. Controls of strike-slip fault on fractures: Insight from 3D discrete element simulation. Science China Earth Sciences, 67(1): 146–164.
Zhang, H.L., Zhang, R.H., Yang, H.J., Shou, J.F., Wang, J.P., Liu, C., and Chen, G., 2014. Characterization and evaluation of ultra-deep fracture-pore tight sandstone reservoirs: A case study of Cretaceous Bashijiqike Formation in Kelasu tectonic zone in Kuqa foreland basin, Tarim, NW China. Petroleum Exploration and Development, 41(2): 175–184.
Zhang, L.K., Luo, X.R., Ye, M.Z., Zhang, B.S., Wei, H.X., Cao, B.F., Xu, X.T., Liu, Z.D., Lei, Y.H., and Li, C., 2021. Small-scale diagenetic heterogeneity effects on reservoir quality of deep sandstones: A case study from the Lower Jurassic Ahe Formation, eastern Kuqa Depression. Geofluids, 2021(1): 6626652.
Zhang, R.H., Yang, H.J., Wang, J.P., Shou, J.F., Zeng, Q.L., and Liu, Q., 2014. The formation mechanism and exploration significance of ultra-deep, low-porosity and tight sandstone reservoirs in Kuqa depression, Tarim basin. Acta Petrolei Sinica, 35(6): 1057–1069 (in Chinese with English abstract).
Zhang, R.H., Wang, K., Zeng, Q.L., Yu, C.F., and Wang, J.P., 2021. Effectiveness and petroleum geological significance of tectonic fractures in the ultra-deep zone of the Kuqa foreland thrust belt: A case study of the Cretaceous Bashijiqike Formation in the Keshen gas field. Petroleum Science, 18(3): 728–741.
Zhao, L.B., Zhang, T.H., Yang, X.J., Guo, X.B., and Rao, H.W., 2018. Gas–water distribution characteristics and formation mechanics in deep tight sandstone gas reservoirs of Keshen block, Kuqa depression, Tarim basin. Natural Gas Geoscience, 29(4): 500–509 (in Chinese with English abstract).
Zhou, M.F., Li, X.Z., Hu, Y., Xu, X., Jiang, L.J., and Li, Y.L., 2021. Physical simulation experimental technology and mechanism of water invasion in fractured-porous gas reservoir: A review. Energies, 14(13): 3918.

About the first author

XU Xiaotong, male, born in 1996 in Yangzhou, Jiangsu Province; Ph.D. candidate from China University of Petroleum (Beijing), Beijing, China. He is now interested in the formation mechanisms of ultra-deep tight sandstone reservoir. E-mail: xxt961961@outlook.com.

About the corresponding author

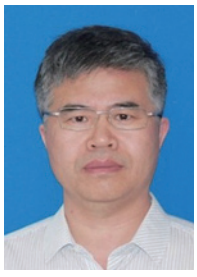

ZENG Lianbo, male, bore in 1967 in Yuanjiang, Hunan Province. He is a professor of Department of Petroleum Exploration and Development Geology in the China University of Petroleum (Beijing). He received his Ph.D. from the China University of Petroleum (Beijing). His interests include tectonic stress fields, natural fracture systems, and low-permeability reservoir characterization. E-mail: lbzeng@sina.com.